Pose error compensation for performance-oriented view planning

Scott, William

https://doi.org/10.4224/8914403

National Research Council Canada
Conseil national de recherches Canada

Institute for Information Technology
Institut de technologie de l'information

NRC · CNRC

Pose Error Compensation for Performance-Oriented View Planning *

Scott, W.R.
August 2004

* published as NRC/ERB-1114. August 18, 2004. NRC 47175.

Canada

National Research Council Canada
Conseil national de recherches Canada

ERB-1114

Institute for Information Technology
Institut de technologie de l'information

NRC-CNRC

Pose Error Compensation for Performance-Oriented View Planning

Scott, W.R.
August 2004

Canada

NRC-47175

Pose Error Compensation for Performance-Oriented View Planning

William R. Scott[†]

[†] Computational Video Group,
National Research Council of Canada, Ottawa, Canada, K1A 0R6
william.scott@nrc-cnrc.gc.ca

Abstract

Automated 3D object reconstruction or inspection using a range camera requires a positioning system to configure sensor-object relative geometry in a sequence of poses defined by a computed view plan. Discrepancies between commanded and actual poses can result in scanning deficiencies. This paper presents a statistically-based method to mitigate pose error effects on a view plan for a common type of range sensor and a generic positioning system. The technique is generalizable to other sensor and positioning system types.

1 Introduction

Active laser scanning range cameras [1] are widely used for high quality 3D object reconstruction and inspection. These processes involve planning views, physically altering the sensor-object pose, taking scans, registering the geometric data in a common reference frame and integrating range images into a non-redundant model. Automating the view planning task remains an open problem. An in-depth discussion of the view planning problem, related issues and a literature survey can be found at [7].

The objective of any view planning technique is to produce a view plan or next-best-view (NBV) list. When the NBV list is sent to a positioning system whose accuracy is inferior to that of the sensor, the coverage of individual viewpoints and of the view plan as a whole is compromised. Individual viewpoint positions and orientations are corrupted. Image coverage (frustum occupancy), visibility, measurement precision and sampling density are effected.

We can recover refined pose estimates post-facto with suitable registration techniques and subsequently re-estimate measurement quality within acquired images. However, the acquired data remains different from that planned. As pose error deteriorates, the computationally intensive view planning phase is progressively compromised - ultimately to be rendered futile. Consequently, there is a need to make the view planning process robust with respect to pose error.

Pose error effects on a view plan have been analyzed in-depth at [5] and summarized at [6]. This paper builds on the previous analysis to present a method of pose error compensation based on a statistical analysis of pose error effects on a common type of range camera and a generic positioning system.

The paper is organized as follows. Section 2 describes the performance-oriented approach to view planning and defines the system models. Section 3 summarizes the analysis of pose error effects reported in earlier work. Section 4 introduces our approach to pose error compensation while deferring details to Appendix A. Experimental results are reported in Section 5. Section 6 concludes the paper.

2 Imaging Environment Models

Performance-oriented view planning [4] begins with a model specification containing explicit, quantified quality objectives for the task - for example, measurement precision and sampling density. This specification-based approach to view planning requires good system models: a sensor model describing camera and frustum geometry and characterizing measurement performance within the calibrated region, plus a positioning system model describing the degrees of freedom, range of motion and positioning performance within the calibrated movement envelope.

Our technique for performance-oriented view planning is presented at [4]. Estimated measurability is computed for viewpoint and target surface point combinations and recorded in a measurability matrix. Each measurability matrix element is a binary estimate of frustum occupancy, bi-static visibility and specification compliance based on approximate knowledge of the imaging environment. Measurability terms and performance measures are defined at [4].

2.1 Sensor Performance Model

We use a comprehensive sensor model in which scanning mechanisms and frustum shapes are defined and parameterized. The camera is modeled as a bi-static sensor with a specified optical baseline. Image size and other parameters are optionally reconfigurable. The model incorporates effects related to bi-static visibility, standoff distance, scanning and grazing angles.

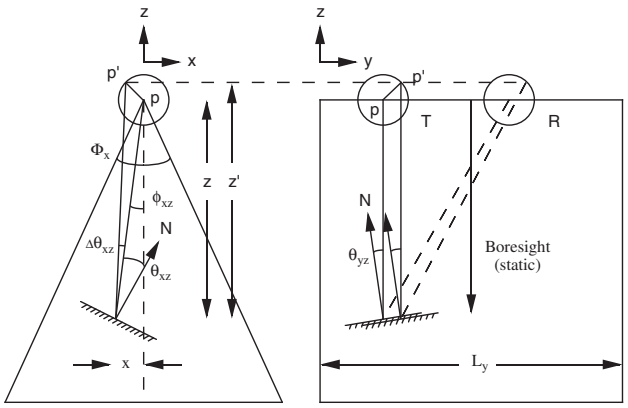

Figure 1: Line-scan Range Camera Geometry

Range Camera Geometry We have modeled several generic range camera designs. The analysis and experimental results presented in this paper are given for a common a common configuration, the line-scan camera, whose imaging geometry is shown at Figure 1. By convention, the camera axis defines the negative z-axis. The negative sign is dropped when referring to range. The frustum for a line-scan camera is defined by Φ_x (x-z plane angular field of view), L_y (y-z plane linear scan length) and R_{min} and R_{max} (minimum and maximum scanning ranges). The transmitter (laser) and receiver (detector) are separated by the optical baseline b along the y-axis. Scanning occurs optically in the x-z plane, where ϕ_{xz} is the instantaneous laser scan angle. In the y-z plane, scanning occurs by mechanical movement of the camera along the y-axis. The foregoing sensor model captures the most important first order sensing mechanisms.

Measurement Precision Based on calibration data [3], we estimate residual random geometric noise statistics as $\hat{\sigma}_x = C_x z, \hat{\sigma}_y = C_y z, \hat{\sigma}_z = C_z z^2$. In the foregoing, $\hat{\sigma}_x, \hat{\sigma}_y, \hat{\sigma}_z$ are standard deviation estimated geometric noise components, noise coefficients (C_x, C_y, C_z) are derived from calibration data and z is range along the camera boresight. As noise along the sensor boresight predominates, we use $\hat{\sigma}_z$ as a surrogate for measurement precision. Estimated sensor noise is further modified by an experimentally-based grazing angle model. Incidence angle effects are most noticeable in the plane of triangulation, the yz-plane, where they generally follow an inverse cosine relationship up to a cut-off angle t_{yz} due to distortion of the shape of the envelope of received energy on the camera detector. There is no noticeable inclination effect in the scanning plane up to a cut-off angle t_{xz} at which point the received energy drops below threshold. Typical thresholds[1] are $t_{yz} = 60°$ and $t_{xz} = 70°$. Thus, we model estimated precision as follows, where $U_i(\theta)$ is the inverse unit step function, i.e. $U_i(\theta) = 1 - U(\theta)$:

$$\hat{\sigma}_z = \frac{C_z z^2}{\cos\theta_{yz}\ U_i(|\theta_{yz}| - t_{yz})\ U_i(|\theta_{xz}| - t_{xz})}. \quad (1)$$

Sampling Density We use a conservative chord-based sampling density estimate $\hat{\rho}_z$, where δx and δy are sampling intervals in the sensor x- and y-axes. Then,

$$\hat{\rho}_z = \frac{1}{\delta x^2 + \delta y^2} \quad (2)$$

$$\text{where } \delta x = R_{xz} \frac{\Phi_x}{N_x - 1} \frac{1}{\cos\theta_{xz}} \quad (3)$$

$$\text{and } \delta y = \frac{L_y}{N_y - 1} \frac{1}{\cos\theta_{yz}}. \quad (4)$$

In Equation 3, $R_{xz} = z/\cos\phi_{xz}$ is the slant range, $\Phi_x/(N_x - 1)$ is the angular sampling interval and $1/\cos\theta_{xz}$ is the inclination effect in the x-z plane. In Equation 4, $L_y/(N_y - 1)$ is the linear sampling interval and $1/\cos\theta_{yz}$ is the inclination effect in the y-z plane. Image size is N_x-by-N_y samples. Adopting abbreviated notation $C\theta = \cos\theta$, etc., the estimated sampling density is

$$\hat{\rho}_z = \frac{(N_x - 1)^2 (N_y - 1)^2 C^2\theta_{xz} C^2\theta_{yz}}{{R_{xz}}^2 {\Phi_x}^2 (N_y - 1)^2 C^2\theta_{yz} + {L_y}^2 (N_x - 1)^2 C^2\theta_{xz}}. \quad (5)$$

2.2 Positioning System Error Model

A variety of positioning systems are in common usage, covering a wide range of accuracy. These include co-ordinate measuring machines (CMMs), translation stages, turntables and robot arms. At the top end, CMMs offer accuracy superior to the best range camera. At the other extreme, robot arms provide good repeatability but poor accuracy relative to high quality range cameras.

It is difficult to characterize accuracy of positioning systems with multiple degrees of freedom [2, 8, 9]. We therefore adopt a simplified pose error model [6]. As with the sensor, we assume calibration removes systemic errors, leaving only residual stochastic errors.

[1] For view planning, we model grazing angle thresholds as hard limits, whereas in practice transitions are more gradual.

Errors in sensor position, boresight axis and rotation about the boresight (twist) are considered to be independent random processes. Position error is modeled as a 3D vector uniformly distributed in direction, whose magnitude is a zero-mean Gaussian process with standard deviation σ_p. Axis error is modeled by a unit vector uniformly distributed on a cone centered on the camera boresight where the cone half-angle is a zero-mean Gaussian process with standard deviation σ_a. Twist error is modeled as a zero-mean Gaussian process with standard deviation σ_t. Currently, our algorithm assumes constant pose error statistics over the movement envelope. However, non-uniform pose error performance can be readily accommodated.

This generic error model is suitable for analyzing pose error effects and corresponding pose error compensation. We have assumed independent position, boresight axis and boresight twist error mechanisms in order to examine the separate effects of these error components. In practical application, it will be necessary to apply a specific error model tailored to the type, configuration and movement envelope of the unique positioning system in actual use.

3 Pose Error Effects

Our analytical and experimental examination of pose error effects on range sensing [5, 6] has shown the phenomena to be highly complex. Effects of pose position error on a single view are minor while pose orientation errors can seriously degrade the acquired image. Axis orientation error is particularly troublesome as the effects are amplified by standoff range. Twist orientation error effects are amplified by the length of the sensor baseline but their impact is minor at the levels of pose error under consideration.

Due to view plan redundancy, partial-to-complete masking of pose error effects is found at low error levels [6]. Further pose error deterioration leads to a rapid decrease in average measurability and increase in measurability variance. As the penalty for coverage failure is typically high for reconstruction and inspection tasks, such unpredictability may be unacceptable.

4 Pose Error Compensation

The problem of pose error effects and their compensation has received scant attention. Tarabanis et al [10] use a synthesis approach for generalized viewpoints which seeks to centralize viewpoints in the admissible domain. Tarbox [11] uses morphological erosion of viewpoints on the periphery of viewpoint sets to reduce vulnerability to pose error. While useful, neither approach is based on objective performance criteria nor analysis of the actual error mechanisms.

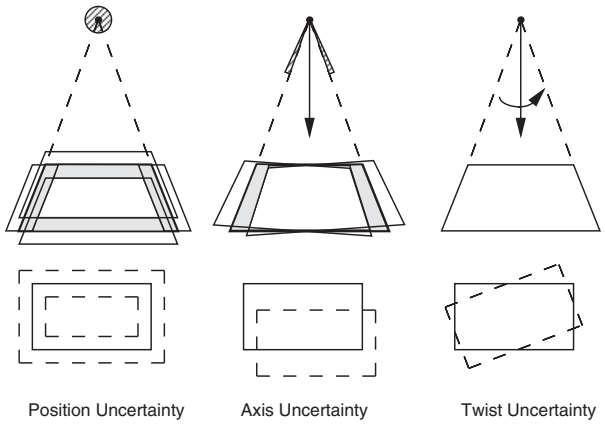

Figure 2: Frustum Erosion with Pose Uncertainty

Pose error affects all three measurability tests: estimation of frustum occupancy, visibility and specification compliance (measurement precision and sampling density). At pose error levels to be reasonably expected, the impact on specification compliance estimation is subtle. The impact on visibility estimation is also subtle and is determined by object shape and imaging geometry. The greatest impact is on frustum occupancy (Figure 2).

Two mechanisms can mitigate pose error effects - (1) view plan redundancy and (2) conservative adjustments to the estimation processes for frustum occupancy, specification compliance and visibility.

View plan redundancy has a major mitigating effect. Complex object shapes are less vulnerable to pose error effects because shape complexity drives view plan redundancy. Conversely, simple object shapes are more vulnerable to pose error as they can be scanned by shorter, more efficient view plans with lower levels of viewpoint correlation.

Based on a statistical analysis of pose error effects [6], our pose error compensation scheme (details at Appendix A) makes allowances for the impact of pose error on estimation of frustum occupancy and specification compliance. We do not presently compensate for the impact on visibility estimation, but this could be easily added. The compensation process applies a reduced frustum volume and more stringent specification compliance tests. We adjust these parameters by user-selected percentage compensation factors applied to the computed impact on the average and standard

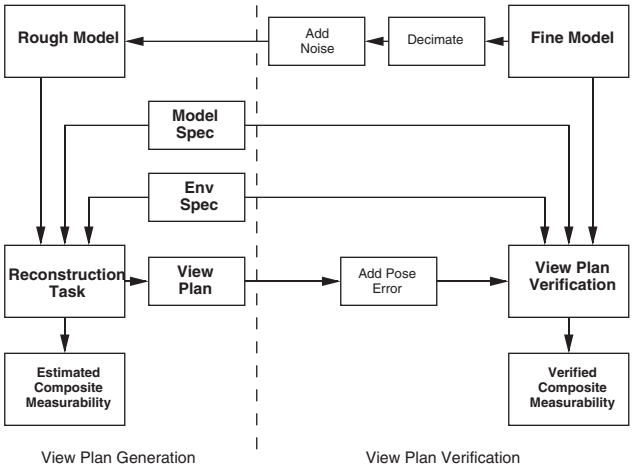

Figure 3: Experimental Process - Measurability Verification

deviation values of frustum and measurability parameters. As the experimental results in the next section illustrate, this approach to pose error compensation can reduce average pose error effects over many trials, but variability remains between individual trials.

5 Experimental Results

5.1 Experimental Process

Our approach to examining the view planning problem has been to use a high fidelity closed loop simulation (Figure 3) which begins with a model specification, an imaging environment specification (range camera and positioning system) and a detailed object model acquired by a high performance range camera. To simulate rough model acquisition, the fine model is decimated and sampling noise is optionally added. A view plan is computed by the modified measurability matrix (3M) algorithm [4] and corrupted with pose error. The loop is subsequently closed by executing the noisy view plan against the original fine model. Finally, performance measures are computed.

For these experiments, two range cameras were modeled (Table 1). Both are line-scan configurations but use different range measurement technology. Sensor 1 is an early generation commercial implementation of the Biris scanning principal and is characterized by a larger optical baseline and depth of field. In comparison, sensor 2, an early generation autosynchronized scanner, exhibits a shorter optical baseline, narrower depth of field and larger range image size.

Specification	Sensor 1	Sensor 2
XZ-plane FOV (Φ_x)	27°	24°
Optical baseline (b)	180_{mm}	100_{mm}
Min Range (R_{min})	142_{mm}	205_{mm}
Max Range (R_{max})	407_{mm}	265_{mm}
YZ-plane max scan length(L_y)	300_{mm}	200_{mm}
Max image size (rangels)	256x256	1024x1024

Table 1: Range Sensor Specifications

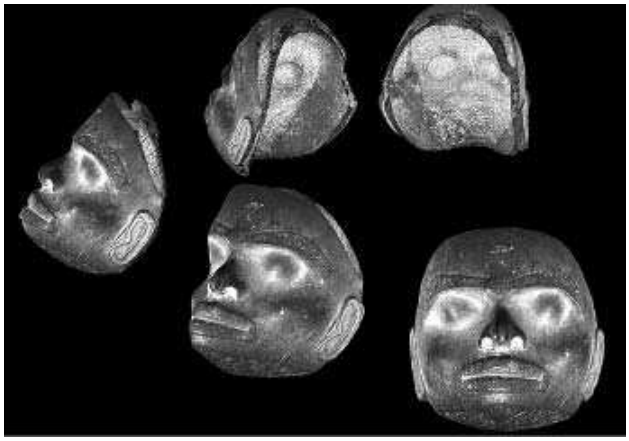

Figure 4: Tsimshian Stone Mask

A description of these technologies can be found at www.vit.iit.nrc.ca/VIT.html.

5.2 Mask Object

Featuring several smaller cavities and ridges within the main steep-walled cavity, the rear segment of the Tsimshian stone mask[2] (Figure 4) presented a difficult view planning challenge for sensor 1, a long baseline range camera. Measurement precision of 50 μm and sampling density of 2 $s/_{mm^2}$ were specified. Surface sampling noise was not added in the trials reported here but pose error was introduced for a second set of experiments. Viewpoints were generated following the "variable" algorithm [4].

In the absence of sampling or pose errors, the view plan of size $n_{gs} = 7$ computed by the variable algorithm with greedy search set covering resulted in verified measurability of $m_v = 0.9807$ with respect to the

[2]The Tsimshian stone mask is regarded as a masterpieces of northwest coast art in the collection of the Canadian Museum of Civilization (VII-C-329). It was collected at the Tsimshian village of Kitkatla in 1879 by I.W. Powell.

View plan	Comp.	Measur. (average)	Measur. (std dev)
$n_{Best} = 5$	0%	$\overline{m_v} = 0.9523$	$\sigma_{m_v} = 0.0120$
$n_{gs} = 7$	0%	$\overline{m_v} = 0.9664$	$\sigma_{m_v} = 0.0123$

Table 2: Verified Measurability - Mask with Pose Error, no Compensation

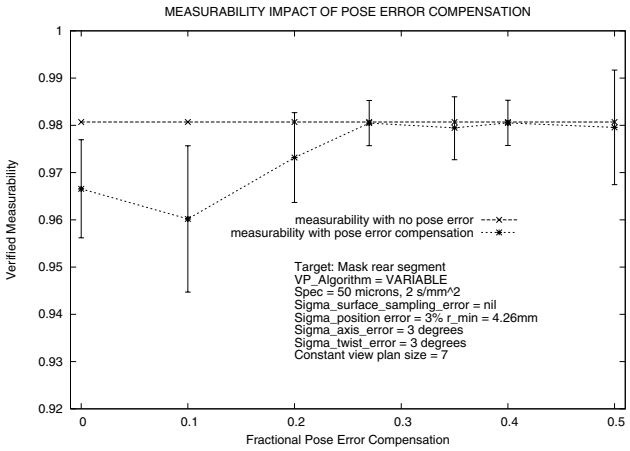

Figure 5: Pose Error Compensation for Mask, View Plan Size 7

specified measurement goals. All surface points are measured within specification excepting a few spots on the steep side walls of the main cavity which are beyond the reach of this long baseline sensor. The shortest view plan found by other set covering methods (size $n_{Best} = 5$) produced a verified measurability of $m_v = 0.9663$. The efficiency of these plans is, respectively, $e_v = 5/7 = 0.714$ and $e_v = 5/5 = 1.0$.

Next, the computed view plan was corrupted by pose error (pose position error $3\%R_{min} = 4.26_{mm}$, pose axis error 3° and pose twist error 3°) using the generic pose error model described in Section 2.2. Table 2 shows average and standard deviation verified measurability in the presence of pose error without pose error compensation.

Pose error compensation was then introduced. Figures 5 and 6 show verified measurability as a function of pose error compensation at a constant view plan length of $n_{gs} = 7$ and $n_{Best} = 5$, respectively. In both cases, the data shows average measurability plus or minus one standard deviation for 20 trials at each compensation level.

Figure 7 illustrates how view plan efficiency de-

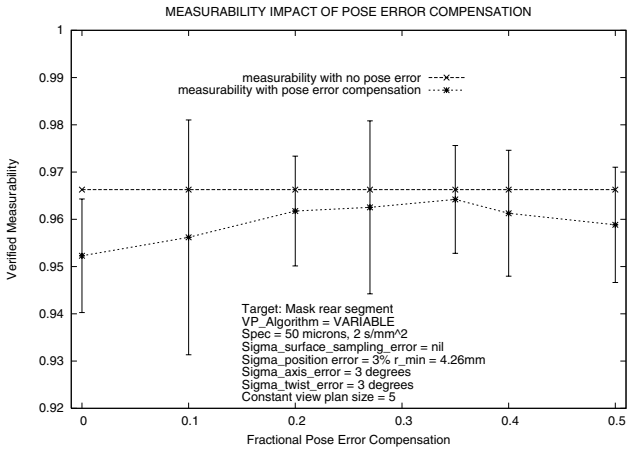

Figure 6: Pose Error Compensation for Mask, View Plan Size 5

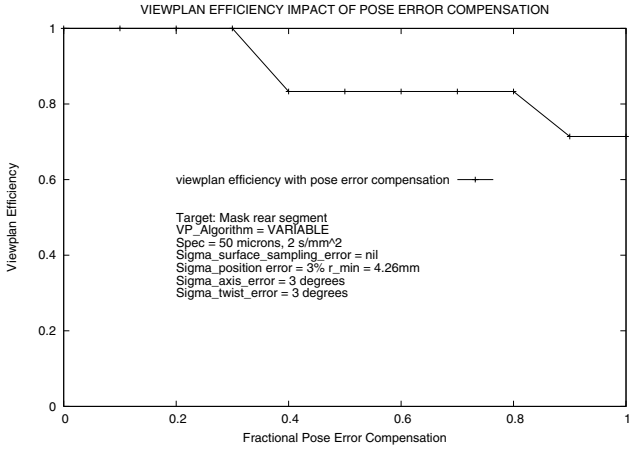

Figure 7: View Plan Efficiency Impact of Pose Error Compensation

View plan	Comp.	Measur. (average)	Measur. (std dev)
$n_{Best} = 5$	35%	$\overline{m_v} = 0.9642$	$\sigma_{m_v} = 0.0114$
$n_{gs} = 7$	35%	$\overline{m_v} = 0.9795$	$\sigma_{m_v} = 0.0066$

Table 3: Verified Measurability - Mask with Pose Error Compensation

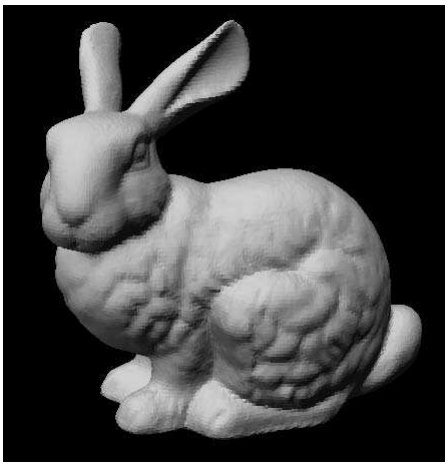

Figure 8: Bunny

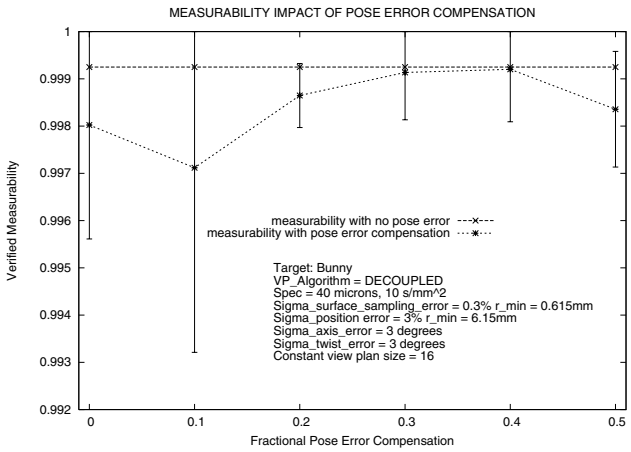

Figure 9: Pose Error Compensation for Bunny, View Plan Size 16

creases with pose error compensation, motivating selection of a modest compensation level. Table 3 shows the impact of a 35% level of pose error compensation for the same level of positioning system error. Compensation allows us to recover, on average, almost the same level of measurement performance as in the absence of pose error. Measurement variability remains between trials, however.

View plan	**Comp.**	**Measur. (average)**	**Measur. (std dev)**
$n_{Best} = 16$	0%	$\overline{m_v} = 0.9978$	$\sigma_{m_v} = 0.0029$
$n_{Best} = 16$	40%	$\overline{m_v} = 0.9992$	$\sigma_{m_v} = 0.0011$

Table 4: Verified Measurability - Bunny with Pose Error Compensation

5.3 Bunny Object

The second test object, the well known bunny (Figure 8), also represents an interesting view planning problem. The most obvious challenge arises from difficult self-occlusion problems in the vicinity of closely-spaced, large protuberances (the ears). Less obvious, but just as difficult, are subtle shadowing problems around a variety of folds and creases in the bunny's fur as well as small crevices around the legs, feet, chin, ears and tail. The sensor's shallow depth of field presents an additional view planning challenge. The model specification called for measurement precision of 40 μm and sampling density of 10 $s/_{mm^2}$. Segmentation was not used and view plans were computed for the object as a whole. Viewpoints were generated following the "decoupled" algorithm [4].

In a baseline experiment without sampling or pose errors, the greedy search view plan of size $n_{gs} = 18$ computed by the decoupled algorithm resulted in verified measurability of $m_v = 1.0$ with respect to the specified measurement goals. The shortest view plan found by other set covering methods (size $n_{Best} = 16$) also produced a verified measurability of $m_v = 1.0$. Respectively, the efficiency of these plans is $e_v = 0.889$ and $e_v = 1.0$.

Next, surface sampling noise was added at a level of $0.3\%R_{min} = 0.615_{mm}$. Pose error was not added at this stage. The decoupled algorithm produced view plans of $n_{gs} = 20$ with $m_v = 1.0$, $e_v = 0.8$ and size $n_{Best} = 16$ with $m_v = 0.9993$, $e_v = 1.0$. While less efficient, it can be seen that the level of redundancy inherent with a greedy search set covering protects against modest levels of rough model sampling error.

Maintaining the rough model sampling error, we next added pose error at the level of position error $3\%R_{min} = 6.15_{mm}$, pose axis error 3° and pose twist error 3°. Figure 9 shows verified measurability as a function of pose error compensation at a constant view plan length of $n_{Best} = 5$. For these experiments, 40 trials were conducted at each compensation level.

Table 4 shows verified measurability statistics for the most efficient view plan at the specified level of sampling error and pose error, with and without pose error compensation. Again, pose error compensation recovers average measurability performance to almost the pose error free case, but variability remains.

6 Summary and Conclusions

Pose error corrupts the output of the computationally expensive view planning phase of object reconstruction or inspection. View plan redundancy and conservative adjustments to the estimation processes for frustum occupancy, specification compliance and visibility can mitigate pose error effects. Perversely, improvements to view plan efficiency result in greater vulnerability to pose error due to the lower level of viewpoint correlation. Pose error vulnerability is also inversely related to object shape complexity.

Our pose error compensation scheme begins with mathematical models of sensor and positioning system performance derived from system design and calibration data. In this paper we have modeled a common type of range sensor and a generic positioning system. The technique is generalizable to other sensor and positioning system types. Given these models, we derive objective compensation measures from a statistical analysis of pose error effects on the modeled system. We compensate for pose error by applying a reduced frustum volume and more stringent specification compliance tests. We adjust these parameters by user-selected percentage compensation factors applied to the computed impact on the average and standard deviation values of frustum and measurability parameters. Generally, a low compensation level is selected, typically 20% - 40%, because we also seek to maintain view plan efficiency. Too high a compensation value unnecessarily drives up view plan length. The current approach balances the beneficial effects of inherent view plan redundancy with statistically-based measurability parameter adjustment.

For geometrically complex shapes, most immunity to pose error arises from view plan redundancy. While the benefits of pose error compensation are small, they are never-the-less beneficial, particularly for repetitive execution of a view plan, such as for inspection applications. This approach to pose error compensation can reduce average pose error effects over many trials, but variability remains between individual trials. Appropriate system design should first specify positioning system performance compatible with the target measurement precision and sampling density goals. Pose error compensation can then be applied to further mitigate pose error effects.

A Compensation Analysis

This appendix extends the analysis of pose error effects at [5] to derive measures directly applicable to pose error compensation. Pose error adversely impacts the ability to make reliable estimates of frustum occupancy, measurement specification compliance and feature visibility. Our present implementation uses this analysis to partially compensate for the first two of these effects. Compensation for the impact on visibility estimation could be easily implemented, but the benefit would be minor.

A.1 Frustum Occupancy

The camera frustum is specified by its field-of-view (FOV) and depth-of-field (DOF). The FOV of a line-scan camera is determined by Φ_x and L_y while the DOF is determined by R_{min} and R_{max} (Section 2.1). We begin by determining the impact of pose error on these frustum parameters. Unless otherwise stated, calculations are for one-sided frustum erosion.

Pose error in sensor position, axis and twist angle $(\sigma_p, \sigma_a, \sigma_t)$ erodes the frustum by $\vec{e} = (e_x, e_y, e_z)$. The one-sided x-axis frustum erosion is $e_x = (e_{x_p}, e_{x_a}, e_{x_t})$ due to the various pose error components. Frustum erosion for the y- and z-axes is similarly defined.

A.1.1 Pose Position Error

From [5], page 11, pose position error $\vec{p} = (p_x, p_y, p_z)$ erodes frustum coverage as follows, where $T\Phi_2 = \tan(\Phi_x/2)$:

$$(e_{x_p}, e_{y_p}, e_{z_p}) = (|p_x| + 2T\Phi_2|p_z|, |p_y|, |p_z|). \quad (6)$$

Using the analysis of [5], we can then readily compute the statistics of these error components:

$$\begin{aligned} \mu_{e_{x_p}} &= (1 + 2T\Phi_2)\sigma_p\sqrt{\frac{2}{3\pi}}, \\ \mu_{e_{y_p}} &= \sigma_p\sqrt{\frac{2}{3\pi}}, \\ \mu_{e_{z_p}} &= \sigma_p\sqrt{\frac{2}{3\pi}}, \end{aligned} \quad (7)$$

and

$$\begin{aligned} {\sigma_{e_{x_p}}}^2 &= \frac{(\pi-2)}{3\pi}{\sigma_p}^2(1 + 4T^2\Phi_2), \\ {\sigma_{e_{y_p}}}^2 &= \frac{(\pi-2)}{3\pi}{\sigma_p}^2, \\ {\sigma_{e_{z_p}}}^2 &= \frac{(\pi-2)}{3\pi}{\sigma_p}^2. \end{aligned} \quad (8)$$

A.1.2 Pose Axis Error

From [5], pages 12 and 15, pose axis error erodes frustum coverage in the vicinity of the boresight as follows:

$$(e_{x_a}, e_{y_a}, e_{z_a}) = (f_d R_o |S\alpha C\beta|, f_d R_o |S\alpha S\beta|, (C\alpha - 1) f_d R_o). \tag{9}$$

From [5], the statistics of these error components are:

$$\begin{aligned} \mu e_{x_a} &= \frac{2 f_d R_o}{\pi} \sigma_a \sqrt{\frac{2}{\pi}}, \\ \mu e_{y_a} &= \frac{2 f_d R_o}{\pi} \sigma_a \sqrt{\frac{2}{\pi}}, \\ \mu e_{z_a} &= -\frac{{\sigma_a}^2}{2} f_d R_o, \end{aligned} \tag{10}$$

and

$$\begin{aligned} {\sigma e_{x_a}}^2 &= {f_d}^2 {R_o}^2 {\sigma_a}^2 (\frac{\pi^3 - 16}{2\pi^3}), \\ {\sigma e_{y_a}}^2 &= {f_d}^2 {R_o}^2 {\sigma_a}^2 (\frac{\pi^3 - 16}{2\pi^3}), \\ {\sigma e_{z_a}}^2 &= {f_d}^2 {R_o}^2 \frac{{\sigma_a}^4}{2}. \end{aligned} \tag{11}$$

A.1.3 Pose Twist Error

As seen from Figure 10, twist error has no impact on DOF coverage, while the impact on x-axis and y-axis coverage is non-uniform. We can approximate the average one-sided width reduction by $A_1/L = \delta W$ and the average one-sided length reduction by $A_2/W = \delta L$. To compute the areas of these triangles, we have the relationships

$$\frac{d_x}{d_y} = T\alpha = \frac{a}{b}, \tag{12}$$

$$\frac{W/2}{a + W/2} = C\alpha. \tag{13}$$

Making the further abbreviation $S = S\alpha$, etc.,

$$a = \frac{W}{2} \frac{(1 - C)}{C} \tag{14}$$

and

$$b = \frac{a}{T} = \frac{W}{2} \frac{(1 - C)}{S}. \tag{15}$$

Then,

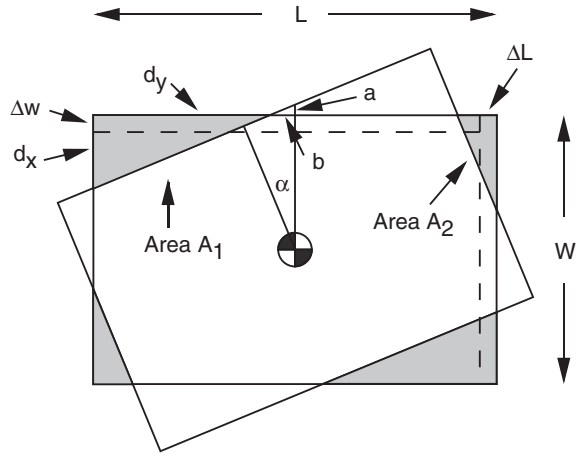

Figure 10: Field-of-View Erosion with Twist Error

$$\begin{aligned} d_y &= \frac{L}{2} - b \\ &= \frac{L}{2} - \frac{W}{2} \frac{(1 - C)}{S} \\ &= \frac{1}{2S}(LS - W + WC) \end{aligned} \tag{16}$$

and

$$\begin{aligned} d_x &= T d_y \\ &= \frac{1}{2C}(LS - W + WC). \end{aligned} \tag{17}$$

So, the area of triangle A_1 is

$$\begin{aligned} A_1 &= \frac{1}{8SC}(LS - W + WC)^2 \\ &= \frac{1}{8SC}(L^2S^2 + W^2 + W^2C^2 \\ &\quad -2LWS + 2LWCS - 2W^2C) \end{aligned} \tag{18}$$

and the area of triangle A_2 is

$$\begin{aligned} A_2 &= \frac{1}{8SC}(WS - L + LC)^2 \\ &= \frac{1}{8SC}(W^2S^2 + L^2 + L^2C^2 \\ &\quad -2LWS + 2LWCS - 2L^2C). \end{aligned} \tag{19}$$

Then,

$$\begin{aligned}\delta W &= \frac{A_1}{L} \\ &= \frac{1}{8SCL}(L^2S^2 + W^2 + W^2C^2 \\ &\quad -2LWS + 2LWCS - 2W^2C) \qquad (20)\end{aligned}$$

and

$$\begin{aligned}\delta L &= \frac{A_2}{W} \\ &= \frac{1}{8SCW}(W^2S^2 + L^2 + L^2C^2 \\ &\quad -2LWS + 2LWCS - 2L^2C). \qquad (21)\end{aligned}$$

For small α, $C = C\alpha \approx 1$, so

$$\delta W \approx \frac{LS}{8}, \qquad (22)$$

and

$$\delta L \approx \frac{WS}{8}. \qquad (23)$$

Then, pose twist error erodes frustum coverage approximately as follows:

$$\begin{aligned}(e_{x_t}, e_{y_t}, e_{z_t}) &= (|\delta W|, |\delta L|, 0) \\ &= (\frac{L|S|}{8}, \frac{W|S|}{8}, 0). \qquad (24)\end{aligned}$$

Using the analysis of [5], we can then readily compute the statistics of these error components:

$$\begin{aligned}\mu e_{x_t} &= \frac{L}{8}\sigma_t\sqrt{\frac{2}{\pi}}, \\ \mu e_{y_t} &= \frac{W}{8}\sigma_t\sqrt{\frac{2}{\pi}}, \\ \mu e_{z_t} &= 0, \qquad (25)\end{aligned}$$

and

$$\begin{aligned}{\sigma e_{x_t}}^2 &= \frac{L^2}{64}{\sigma_t}^2\frac{(\pi-2)}{\pi}, \\ {\sigma e_{y_t}}^2 &= \frac{W^2}{64}{\sigma_t}^2\frac{(\pi-2)}{\pi}, \\ {\sigma e_{z_t}}^2 &= 0. \qquad (26)\end{aligned}$$

The statistics at Equations 25 and 26 can normally be evaluated for the frustum width at the optimum stand-off range $W = 2f_dR_oT\Phi_2$ and the optimized scan length $L = f_dR_o\Phi_x$.

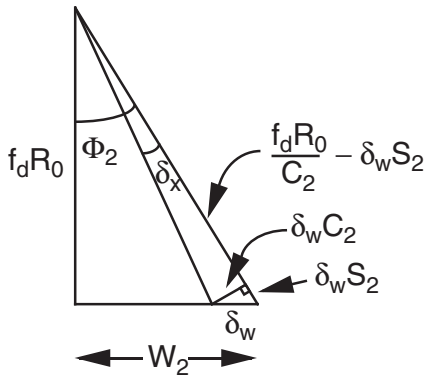

Figure 11: Field-of-View Erosion Geometry

A.1.4 Composite Pose Error

As our pose error model considers errors in sensor position, boresight axis and rotation about the boresight to be independent random processes, the statistics of the composite one-sided frustum erosion are

$$\begin{aligned}\mu e_x &= \mu e_{x_p} + \mu e_{x_a} + \mu e_{x_t}, \\ \mu e_y &= \mu e_{y_p} + \mu e_{y_a} + \mu e_{y_t}, \\ \mu e_z &= \mu e_{z_p} + \mu e_{z_a} + \mu e_{z_t}, \qquad (27)\end{aligned}$$

$$\begin{aligned}{\sigma e_x}^2 &= {\sigma e_{x_p}}^2 + {\sigma e_{x_a}}^2 + {\sigma e_{x_t}}^2, \\ {\sigma e_y}^2 &= {\sigma e_{y_p}}^2 + {\sigma e_{y_a}}^2 + {\sigma e_{y_t}}^2, \\ {\sigma e_z}^2 &= {\sigma e_{z_p}}^2 + {\sigma e_{z_a}}^2 + {\sigma e_{z_t}}^2. \qquad (28)\end{aligned}$$

A.1.5 Frustum Occupancy Compensation

We can then apply compensation (c_x, c_y, c_z) along the frustum x,y,z-axes by fractional amounts f_μ and f_σ. The range of f_μ is $[0, 1]$. In principle, the upper limit on the range of f_σ could be greater than 1. However, our experiments have shown it appropriate to set both factors to a low value, typically in the range $[0.2, 0.4]$.

$$\begin{aligned}c_x &= f_\mu\mu e_x + f_\sigma\sigma e_x, \\ c_y &= f_\mu\mu e_y + f_\sigma\sigma e_y, \\ c_z &= f_\mu\mu e_z + f_\sigma\sigma e_z. \qquad (29)\end{aligned}$$

To compute the effect of x-axis frustum erosion on the sensor field of view Φ_x, refer to Figure 11, where $\delta w = c_x$. Then, $\delta\Phi_x$ is

$$\delta\Phi_x = \arctan\left[\frac{c_x C\Phi_2}{\frac{f_d R_o}{C\Phi_2} - c_x S\Phi_2}\right]. \quad (30)$$

Finally, we compensate for pose error effects by shrinking the frustum through the following changes:

$$\begin{aligned} \Phi_x &\leftarrow \Phi_x - 2\ \delta\Phi_x, \\ L_y &\leftarrow L_y - 2\ c_y, \\ R_{min} &\leftarrow R_{min} + c_z, \\ R_{max} &\leftarrow R_{max} - c_z. \end{aligned} \quad (31)$$

where x,y,z-axes frustum erosion compensation values (c_x, c_y, c_z) are given at Equation 29.

A.2 Specification Compliance

A.2.1 Measurement Precision Estimation Error

In our earlier analysis of the relative effect of pose error [5],[6], it was convenient to define relative estimated measurement precision P_{rel} as the ratio of estimated precision in the case of pose error to estimated precision in the error-free case. Then,

$$P_{rel} = \frac{\hat{\sigma}_{z'}}{\hat{\sigma}_z} = \frac{z'^2}{z^2}\frac{\cos\theta_{yz}}{\cos\theta'_{yz}}. \quad (32)$$

where z' and θ'_{yz} are the range and y-z incidence angle as perturbed by pose error. Temporarily dropping the "z" subscript for simplicity, we let $P_{rel} = \hat{\sigma}'/\hat{\sigma}$. We are interested in the error $e_{\hat{\sigma}}$ in the estimated measurement precision

$$e_{\hat{\sigma}} = \hat{\sigma}' - \hat{\sigma} = \hat{\sigma}(P_{rel} - 1). \quad (33)$$

Consequently, the statistics of measurement precision estimation error due to pose error is simply

$$\frac{\mu e_{\hat{\sigma}}}{\hat{\sigma}} = (\mu_{P_{rel}} - 1), \quad (34)$$

$$\frac{{\sigma e_{\hat{\sigma}}}^2}{\hat{\sigma}^2} = {\sigma_{P_{rel}}}^2. \quad (35)$$

Taking all pose error components into account, the combined impact on measurement precision estimation is

$$\begin{aligned} \frac{\mu e_{\hat{\sigma}}}{\hat{\sigma}} &= (\mu_{P_{rel_p}} - 1) + (\mu_{P_{rel_a}} - 1) + (\mu_{P_{rel_t}} - 1) \\ &= \frac{1}{3{f_d}^2}\frac{{\sigma_p}^2}{{R_o}^2} - \frac{3{\sigma_a}^2}{4}, \end{aligned} \quad (36)$$

$$\begin{aligned} \frac{{\sigma e_{\hat{\sigma}}}^2}{\hat{\sigma}^2} &= {\sigma_{P_{rel_p}}}^2 + {\sigma_{P_{rel_a}}}^2 + {\sigma_{P_{rel_t}}}^2 \\ &= \frac{4}{3{f_d}^2}\frac{{\sigma_p}^2}{{R_o}^2}. \end{aligned} \quad (37)$$

A.2.2 Measurement Precision Compensation

We can apply compensation $c_{\hat{\sigma}}$ to the estimated measurement precision by amounts f_μ and f_σ.

$$c_{\hat{\sigma}} = f_\mu\ \mu e_{\hat{\sigma}} + f_\sigma\ \sigma e_{\hat{\sigma}} \quad (38)$$

We can compensate estimated precision for each measurability matrix element by the adjustment

$$\begin{aligned} \hat{\sigma} &\leftarrow \hat{\sigma} + c_{\hat{\sigma}}, \\ \hat{\sigma} &\leftarrow \hat{\sigma}(1 + f_\mu\frac{\mu e_{\hat{\sigma}}}{\hat{\sigma}} + f_\sigma\frac{\sigma e_{\hat{\sigma}}}{\hat{\sigma}}). \end{aligned} \quad (39)$$

To be compliant, the precision estimate must pass the test $\hat{\sigma} < \sigma_s$, where σ_s is the specified measurement precision. In the presence of pose error, the test becomes $\hat{\sigma}' < \sigma_s$ or

$$\hat{\sigma}(1 + f_\mu\frac{\mu e_{\hat{\sigma}}}{\hat{\sigma}} + f_\sigma\frac{\sigma e_{\hat{\sigma}}}{\hat{\sigma}}) < \sigma_s. \quad (40)$$

Consequently, compensation can be alternately achieved by a single adjustment to the specified measurement precision σ_s.

$$\sigma_s \leftarrow \sigma_s/(1 + f_\mu\frac{\mu e_{\hat{\sigma}}}{\hat{\sigma}} + f_\sigma\frac{\sigma e_{\hat{\sigma}}}{\hat{\sigma}}). \quad (41)$$

A.2.3 Sampling Density Estimation Error

Similarly, in our earlier analysis of the relative effect of pose error [5],[6], it was convenient to define relative estimated sampling density D_{rel} as the ratio of estimated sampling density in the pose error case to estimated sampling density in the error-free case. Then,

$$D_{rel} = \frac{\hat{\rho}_{z'}}{\hat{\rho}_z}. \quad (42)$$

Again temporarily dropping the "z" subscript for simplicity, we let $D_{rel} = \hat{\rho}'/\hat{\rho}$. We are interested in the error $e_{\hat{\rho}}$ in the estimated sampling density

$$e_{\hat{\rho}} = \hat{\rho}' - \hat{\rho} = \hat{\rho}(D_{rel} - 1). \quad (43)$$

The statistics of sampling density estimation error due to pose error is therefore

$$\frac{\mu e_{\hat{\rho}}}{\hat{\rho}} = (\mu_{D_{rel}} - 1), \tag{44}$$

$$\frac{{\sigma e_{\hat{\rho}}}^2}{\hat{\rho}^2} = {\sigma_{D_{rel}}}^2. \tag{45}$$

Taking all pose error components into account, the combined impact on sampling density estimation is

$$\begin{aligned} \frac{\mu e_{\hat{\rho}}}{\hat{\rho}} &= (\mu_{D_{rel_p}} - 1) + (\mu_{D_{rel_a}} - 1) + (\mu_{D_{rel_t}} - 1) \\ &= \frac{1}{3{f_d}^2}\frac{{\sigma_p}^2}{{R_o}^2} - \frac{{\sigma_a}^2}{4}, \end{aligned} \tag{46}$$

$$\begin{aligned} \frac{{\sigma e_{\hat{\rho}}}^2}{\hat{\rho}^2} &= {\sigma_{D_{rel_p}}}^2 + {\sigma_{D_{rel_a}}}^2 + {\sigma_{D_{rel_t}}}^2 \\ &= \frac{2}{3{f_d}^2}\frac{{\sigma_p}^2}{{R_o}^2}. \end{aligned} \tag{47}$$

A.2.4 Sampling Density Compensation

We can apply compensation $c_{\hat{\rho}}$ to the estimated sampling density by amounts f_μ and f_σ.

$$c_{\hat{\rho}} = f_\mu \ \mu e_{\hat{\rho}} + f_\sigma \ \sigma e_{\hat{\rho}} \tag{48}$$

We can compensate estimated sampling density for each measurability matrix element by the adjustment

$$\begin{aligned} \hat{\rho} &\leftarrow \hat{\rho} - c_{\hat{\rho}}, \\ \hat{\rho} &\leftarrow \hat{\rho}(1 - f_\mu \frac{\mu e_{\hat{\rho}}}{\hat{\rho}} - f_\sigma \frac{\sigma e_{\hat{\rho}}}{\hat{\rho}}). \end{aligned} \tag{49}$$

To be compliant, the sampling density estimate must pass the test $\hat{\rho} > \rho_s$, where ρ_s is the specified measurement sampling density. In the presence of pose error, the test becomes $\hat{\rho}' > \rho_s$ or

$$\hat{\rho}(1 - f_\mu \frac{\mu e_{\hat{\rho}}}{\hat{\rho}} - f_\sigma \frac{\sigma e_{\hat{\rho}}}{\hat{\rho}}) > \rho_s. \tag{50}$$

Consequently, compensation can be alternately achieved by a single adjustment to the specified sampling density ρ_s.

$$\rho_s \leftarrow \rho_s / (1 - f_\mu \frac{\mu e_{\hat{\rho}}}{\hat{\rho}} - f_\sigma \frac{\sigma e_{\hat{\rho}}}{\hat{\rho}}). \tag{51}$$

When computing a sampling density estimate for the pose-error-compensated frustum, the effective radial or linear sampling rate should be left unchanged. Let ${\Phi_x}^c$ be the compensated x-z plane angular field of view, ${L_y}^c$ be y-z plane linear scan length and n_x and n_y the number of samples in these planes. For specification compliance testing only, these values should be modified as follows:

$$\begin{aligned} n_x &\leftarrow \lfloor n_x \frac{T{\Phi_2}^c}{T\Phi_2} \rfloor, \\ n_y &\leftarrow \lfloor n_y \frac{{L_y}^c}{L_y} \rfloor. \end{aligned} \tag{52}$$

References

[1] P. Besl. Range image sensors. In J. Sanz, editor, *Advances in Machine Vision*. Springer-Verlag, New York, 1989.

[2] P. Cauchick-Miguel, T. King, and J. Davis. CMM verification: A survey. *Measurement*, 17(1):1–16, 1996.

[3] S. El-Hakim and J.-A. Beraldin. Configuration design for sensor integration. In *Proc. Videometrics IV, SPIE, Philadelphia, Pennsylvania*, volume 2598, pages 274–285, 25-26 October 1995.

[4] W. Scott. Performance-oriented view planning. *Submitted to Computer Vision and Image Understanding*, March 2004.

[5] W. Scott, G. Roth, and J.-F. Rivest. View planning with positioning system error. Technical Report NRC-44195, National Research Council of Canada, Institute for Information Technology, May 2001.

[6] W. Scott, G. Roth, and J.-F. Rivest. Pose error effects on range sensing. In *15th Int. Conf. on Vision Interface, Calgary*, pages 331–338, May 2002.

[7] W. Scott, G. Roth, and J.-F. Rivest. View planning for automated 3D object reconstruction and inspection. *ACM Computing Surveys*, 35(1):64–96, March 2003.

[8] Y. Shin and Y. Wei. A statistical analysis of positional errors of a multi-axis machine tool. *Precision Engineering*, 14(3):139–146, July 1992.

[9] J. Soons, F. Thomas, and P. Schellekens. Modeling the errors of multi-axis machines: A general methodology. *Precision Engineering*, 14(1):5–19, July 1992.

[10] K. Tarabanis, R. Tsai, and P. Allen. The MVP sensor planning system for robotic vision tasks. *IEEE Trans. Robotics and Automation*, 11(1):72–85, February 1995.

[11] G. Tarbox and S. Gottschlich. Planning for complete sensor coverage in inspection. *Computer Vision and Image Understanding*, 61(1):84–111, January 1995.

Pose Error	X-axis Frustum Erosion	Y-axis Frustum Erosion	Z-axis Frustum Erosion
Position	$\mu e_{x_p} = (1 + 2T\Phi_2)\sigma_p\sqrt{\frac{2}{3\pi}}$ $\sigma e_{x_p}{}^2 = \frac{(\pi-2)}{3\pi}\sigma_p{}^2(1 + 4T^2\Phi_2)$	$\mu e_{y_p} = \sigma_p\sqrt{\frac{2}{3\pi}}$ $\sigma e_{y_p}{}^2 = \frac{(\pi-2)}{3\pi}\sigma_p{}^2$	$\mu e_{z_p} = \sigma_p\sqrt{\frac{2}{3\pi}}$ $\sigma e_{z_p}{}^2 = \frac{(\pi-2)}{3\pi}\sigma_p{}^2$
Axis	$\mu e_{x_a} = \frac{2f_dR_o}{\pi}\sigma_a\sqrt{\frac{2}{\pi}}$ $\sigma e_{x_a}{}^2 = f_d{}^2R_o{}^2\sigma_a{}^2(\frac{\pi^3-16}{2\pi^3})$	$\mu e_{y_a} = \frac{2f_dR_o}{\pi}\sigma_a\sqrt{\frac{2}{\pi}}$ $\sigma e_{y_a}{}^2 = f_d{}^2R_o{}^2\sigma_a{}^2(\frac{\pi^3-16}{2\pi^3})$	$\mu e_{z_a} = -\frac{\sigma_a{}^2}{2}f_dR_o$ $\sigma e_{z_a}{}^2 = f_d{}^2R_o{}^2\frac{\sigma_a{}^4}{2}$
Twist	$\mu e_{x_t} = \frac{L}{8}\sigma_t\sqrt{\frac{2}{\pi}}$ $\sigma e_{x_t}{}^2 = \frac{L^2}{64}\sigma_t{}^2\frac{(\pi-2)}{\pi}$	$\mu e_{y_t} = \frac{W}{8}\sigma_t\sqrt{\frac{2}{\pi}}$ $\sigma e_{y_t}{}^2 = \frac{W^2}{64}\sigma_t{}^2\frac{(\pi-2)}{\pi}$	$\mu e_{z_t} = 0$ $\sigma e_{z_t}{}^2 = 0$

Table 5: One-sided Frustum Erosion due to Pose Error

Pose Error	Measurement Precision Estimate Error	Sampling Density Estimate Error
Position	$\frac{\mu e_{\hat{\sigma}}}{\hat{\sigma}} = \frac{1}{3f_d{}^2}\frac{\sigma_p{}^2}{R_o{}^2}$ $\frac{\sigma e_{\hat{\sigma}}{}^2}{\hat{\sigma}^2} = \frac{4}{3f_d{}^2}\frac{\sigma_p{}^2}{R_o{}^2}$	$\frac{\mu e_{\hat{\rho}}}{\hat{\rho}} = \frac{1}{3f_d{}^2}\frac{\sigma_p{}^2}{R_o{}^2}$ $\frac{\sigma e_{\hat{\rho}}{}^2}{\hat{\rho}^2} = \frac{2}{3f_d{}^2}\frac{\sigma_p{}^2}{R_o{}^2}$
Axis	$\frac{\mu e_{\hat{\sigma}}}{\hat{\sigma}} = -\frac{3\sigma_a{}^2}{4}$ $\frac{\sigma e_{\hat{\sigma}}{}^2}{\hat{\sigma}^2} = 0$	$\frac{\mu e_{\hat{\rho}}}{\hat{\rho}} = -\frac{\sigma_a{}^2}{4}$ $\frac{\sigma e_{\hat{\rho}}{}^2}{\hat{\rho}^2} = 0$
Twist	$\frac{\mu e_{\hat{\sigma}}}{\hat{\sigma}} = 0$ $\frac{\sigma e_{\hat{\sigma}}{}^2}{\hat{\sigma}^2} = 0$	$\frac{\mu e_{\hat{\rho}}}{\hat{\rho}} = 0$ $\frac{\sigma e_{\hat{\rho}}{}^2}{\hat{\rho}^2} = 0$

Table 6: Measurement Estimation Errors due to Pose Error

Frustum erosion for twist pose error in Table 5 can normally be evaluated for the frustum width at the optimum stand-off range $W = 2f_dR_oT\Phi_2$ and the optimized scan length $L = f_dR_o\Phi_x$.